Fourier inversion of acoustic wave fields in anisotropic solids

M. Pluta,[1,*] A. G. Every,[1] W. Grill,[2] and T. J. Kim[3]
[1]*School of Physics, University of the Witwatersrand, PO WITS 2050, South Africa*
[2]*Institut fur Experimentelle Physik II, Universitat Leipzig, Linnestrasse 5, D-04103 Leipzig, Germany*
[3]*Technical Institute UVT Co., Ltd., No. 22-6 DangJeung-Dong, Gunpo-City, Kyung Ki-Do, Korea*
(Received 16 August 2002; revised manuscript received 16 December 2002; published 31 March 2003)

This paper is concerned with the analysis of acoustic wave fields encountered in phase-sensitive acoustic microscopy (PSAM) applied to elastically anisotropic solids. We show that the fast Fourier transform technique provides a computationally efficient method of calculating two-dimensional amplitude and phase images of these fields. More importantly, we demonstrate how this technique, applied to complex wave field data, can be used to treat inverse problems such as source reconstruction, image quality assessment, and the determination of elastic constants. Monochromatic and also more general time-dependent excitations, such as tone bursts and short pulses, are treated, and the resulting wave fields described. The evolution of these wave fields with increasing frequency is discussed, and emerging infinite frequency features, such as the ray surface and phonon focusing caustics, are identified. A number of numerical simulations are presented that are in good agreement with measured data from the literature. As an illustration of elastic constant determination, we use the point spread function determination based on our PSAM measurements on the longitudinal mode in silicon to determine the elastic constant C_{11} of Si.

DOI: 10.1103/PhysRevB.67.094117 PACS number(s): 62.65.+k, 43.35.+d

I. INTRODUCTION

There has been sustained interest for a number of years in the pointlike excitation and detection of acoustic wave fields in elastically anisotropic solids using phase-sensitive acoustic microscopy (PSAM) and other means (see, e.g., the reviews in Refs. 1–5, the recent papers,[6,7] and references contained therein). In the case of harmonic or quasiharmonic excitation, the spatial variation of these fields is particularly striking, revealing as it does the combined effects of internal diffraction and phonon focusing. Very-high-frequency images obtained with ballistic phonons display patterns of non-diffraction-broadened caustics that are well accounted for in the ray approximation, but these images are intensity plots, devoid of phase information. In analogous experiments done at MHz ultrasonic frequencies, the caustics unfold into Airy, Pearcey, and higher-order diffraction patterns, which then broaden and merge as the frequency is progressively lowered. As a tradeoff for this loss of detail in the focusing, one is able to retain both phase and amplitude data in internal diffraction images. This is what is done in PSAM,[1] capturing the two-dimensional (2D) complex signal transmitted through a sample. We show in this paper that with combined phase and amplitude data, it is possible to use the angular spectrum approach and the fast Fourier transform (FFT) technique to tackle forward propagation and inversion problems, such as source reconstruction, image quality assessment, and the determination of elastic constants.

Our treatment is based on the Green's function $\tilde{G}_{33}(\vec{x},\omega)$ for an infinitely extended anisotropic elastic continuum, which we evaluate by the angular spectrum method to provide synthetic data for inversion. More general time-dependent forms of excitation, such as tone bursts and short pulse excitation, are also treated, and the resulting wave fields compared. As regards the role of the sample boundaries, in using a focusing transducer of relatively small angular aperture to insonify a solid at normal incidence, the $\vec{k}$-space angular spectrum within the solid does not differ markedly from that resulting from a time-harmonic point force acting along the axial direction in the infinite continuum. For this reason, and also because the thrust of this paper is the demonstration of broad principles, we do not take account of surface effects here. The modifications required to incorporate surfaces into the calculations are relatively straightforward, but we defer them to later presentations.

The layout of this paper is as follows: In Sec. II we describe the PSAM technique and the physical conditions that are achieved with it. In Sec. III we develop the theory for the forward problem of the wave field of a point force with harmonic and more general time dependence. We present a number of numerical simulations for silicon, obtained using FFT's, which are in excellent agreement with measured data available in the literature. In Sec. IV we discuss a spatially distributed source, treating both forward propagation and inversion, and also the issue of image quality determination. In Sec. V we illustrate the potential of our technique for inverse problem solving, by using the point spread function determination from our PSAM measurements on the longitudinal mode in silicon, to determine the elastic constant C_{11} of Si. Finally in Sec. VI we present our conclusions.

II. THE PSAM EXPERIMENTAL TECHNIQUE

PSAM is used for studying the propagation of divergent ultrasonic beams through a solid, usually in the nature of an elastically anisotropic crystal.[1] The acoustical part of the experimental setup in PSAM is shown in Fig. 1. A pair of point-focus transducers, one a transmitter and the other a receiver, is focused through a transmission fluid onto opposite faces of the sample. One of the transducers is raster scanned parallel to the surface, yielding an image of the

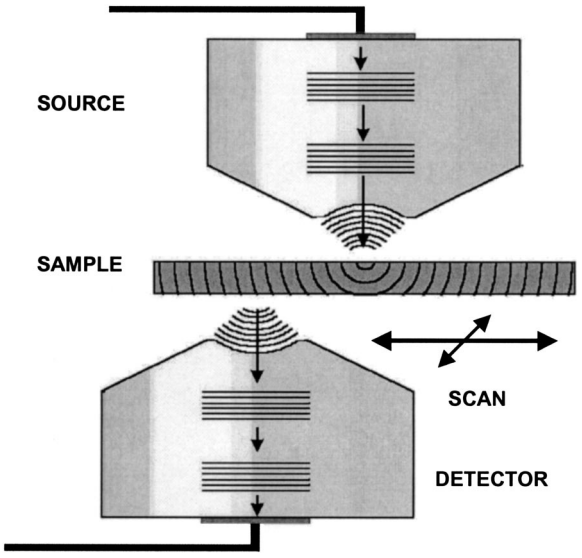

FIG. 1. Schematic representation of the acoustical part of the PSAM experiment (Ref. 1). The ultrasonic signal is generated and detected by a pair of transducers focused on opposite surfaces of the sample. One of the transducers is raster scanned parallel to the sample surface.

transmitted sound field. The system operates on rf signals excited by a narrow-bandwidth cw generator, the output of which is split into the signal that generates the ultrasonic wave and an electronic reference. The transmitted ultrasonic signal is time gated to separate the longitudinal and transversal acoustic modes of propagation and to eliminate multipass echoes. The signal from the ultrasonic path is then mixed in two channels with the electronic reference 0° and 90° phase shifted, and after boxcar averaging, the scheme delivers two low-frequency signals that may be regarded as the real and imaginary parts of the analytical signal pertaining to the ultrasonic wave transmitted through the sample. The two-dimensional map of the amplitude and phase variation of this signal has properties similar to a hologram. Application of this scheme has allowed high-resolution data to be obtained in the gigahertz regime.

By the use of the focusing transducers and the coupling fluid, which transmits only pressure waves, excitation, and detection of displacement normal to the surface of the solid is achieved, which is pointlike to the extent that the lateral sizes of the focal areas on the opposite surfaces of the sample are smaller than the wavelength λ within the sample. The diameter of the Airy disk d_A on the surface in relation to λ is given by

$$d_A/\lambda = \frac{1.22}{\sin(\theta)}\frac{c_w}{c_s}, \tag{1}$$

where c_w and c_s are the sound velocities in the transmission fluid (water) and the sample respectively, and θ is the half aperture angle of the lens. Since in most solids the sound velocity is more than double that of water (in the case of silicon, even for the transversal modes it is closer to a factor of 4), a lens of half aperture angle greater than about 30° is usually adequate for achieving pointlike excitation and consequent propagation in a wide spread of forward directions within the solid.

III. POINT SOURCE: THE FORWARD PROBLEM

To apply the 2D fast Fourier transform in the treatment of wave propagation and "internal diffraction" of acoustic waves in anisotropic solids, we need first of all to explore the link between the strict Green's function approach[8] and the Fourier-transform-based angular spectrum method.[9] From there we proceed to the calculational technique used in the later sections.

A. Time-harmonic point force

We treat, as the forward problem, the displacement field of a time-harmonic point force of angular frequency $\omega = 2\pi f$, acting in the x_3 direction at the origin (0, 0, 0) in an infinitely extensive anisotropic elastic continuum of mass density ρ and elastic stiffness tensor c_{ijkl}. The displacement response in the x_3 direction at a point $\vec{x}$ in the observation plane, which is perpendicular to the x_3 direction, is the dynamic Green's function $\tilde{G}_{33}(\vec{x},\omega)$, which has the integral representation[8]

$$\tilde{G}_{33}(\vec{x},\omega) = \sum_{n=1}^{3}\left\{\frac{i\omega}{8\pi^2\rho}\int_\Omega d\Omega\, s^{(n)3}\Lambda_{33}^{(n)}\exp(i\omega\vec{s}^{(n)}\cdot\vec{x}) + \frac{1}{8\pi^2\rho x}\int_0^{2\pi} d\phi\, s^{(n)2}\Lambda_{33}^{(n)}\right\}, \tag{2}$$

where $\vec{s}^{(n)}$ is the slowness vector associated with the nth acoustic branch: longitudinal (L), fast transverse (FT) and slow transverse (ST), $d\Omega$ is the infinitesimal solid angle in slowness space, and $\Lambda_{33}^{(n)} = [U_3^{(n)}]^2$ is the coupling factor for each mode, with $U_3^{(n)}$ being the x_3 component of the polarization eigenvector.

In the intermediate and far field, where $\omega s x \gg 1$, the second term in Eq. (2), for which the associated strain field falls off as $\sim 1/x^2$, is small compared with the first term, for which the strain field falls off as $\sim 1/x$, and so is neglected below. In many experiments, a wave train of finite duration rather than a perfectly monochromatic source is employed, and time gating is used to separately study the longitudinal and transverse wave fields. In the equations below, we accordingly suppress the polarization index n and summation over that index. The integral over solid angle Ω is readily transformed to a surface integral over (s_1, s_2), yielding

$$\tilde{G}_{33}(\vec{x},\omega) = \frac{i\omega}{8\pi^2\rho}\int ds_1 ds_2 \frac{\Lambda_{33}}{V_3}\exp(i\omega\vec{s}\cdot\vec{x}), \tag{3}$$

where $V_3(\vec{s})$ is the x_3 component of the group velocity or ray vector

$$\vec{V} = \frac{\vec{\nabla}_s S(\vec{s})}{\vec{s}\cdot\vec{\nabla}_s S(\vec{s})}.$$

$\vec{V}$ is normal to the acoustic slowness surface, the surface representing the directional dependence of the slowness $\vec{s}$. To render Eq. (3) more transparently in the form of a Fourier transform, we change the integration variable to wave vector $\vec{k}_\parallel=(k_1,k_2)=\omega\vec{s}_\parallel=\omega\cdot(s_1,s_2)$, yielding

$$\tilde{G}_{33}(\vec{x},\omega)=A\int d\vec{k}_\parallel^{\,2}\left\{\frac{\Lambda_{33}}{V_3}\exp[i\omega x_3 s_3]\right\}\exp(i\vec{k}_\parallel\cdot\vec{x}_\parallel), \tag{4}$$

where $A=i/8\pi^2\rho\omega$, and Λ_{33}, V_3, and s_3 are regarded as functions of $\vec{k}_\parallel/\omega$. In numerical simulations we include in the integrand a slowly varying windowing function $H(\vec{k}_\parallel)$ that could represent the directionality of the transducers and that provides a smooth cutoff to the domain of integration.

The above expression is almost identical to that for the field of a focusing transducer transmitted through a parallel-sided solid, except that in the latter situation, the factor V_3 is absent and $A\Lambda_{33}$ is replaced by the product of the transmission coefficients at the surfaces, which has a similar angular spectral behavior for small $\vec{k}_\parallel$. The results we present here are not very sensitive to the precise form of H, and the difference between the two approaches amounts to not much more than varying the windowing function. More important is the influence of the phase variation associated with the slowness component s_3 in Eq. (4).

B. General time-dependent point force

In the case of excitation by a time-dependent signal $F(t)$ with frequency spectrum $f(\omega)$, the transient response is

$$G_{33}(\vec{x},t)=\int \tilde{G}_{33}(\vec{x},\omega)f(\omega)\exp[-i\omega t]d\omega, \tag{5}$$

where $\tilde{G}_{33}(\vec{x},\omega)$ is given by Eq. (4). If we perform the integration with respect to ω first, this yields the function

$$K(\vec{k}_\parallel,t)=\int d\omega\, f(\omega)\frac{\Lambda_{33}}{V_3}\exp\{i\omega[x_3 s_3-t]\}, \tag{6}$$

for the remaining Fourier transform with respect to $\vec{k}_\parallel$. The advantage of this is that the K functions for the L, FT, and ST modes can be combined at this stage, leading to a significant saving in computational time. We show examples of this type of calculation in Fig. 3.

C. Calculational technique

Equation (4), proposed in simplified form by Pluta *et al.*,[9] is in the form of a Fourier transform, and may be performed numerically by application of the 2D FFT algorithm. This entails numerically solving Christoffel's equation for the slownesses and eigenvectors[10] for an $N\times N$ array of $\vec{k}_\parallel$'s. The subsequent saving in computational time in using a FFT, as compared with a ''classical'' numerical Fourier inversion, is

$$\frac{t_{\mathrm{FFT}}}{t_{\mathrm{cl}}}=\left[\frac{\log_2 N}{2N}\right]^2,$$

which for $N=1024$ comes to $t_{\mathrm{FFT}}/t_{\mathrm{cl}}\approx[1/200]^2$.
In applying a discrete Fourier transform we have to take account of the distribution of sampling points and the bandwidth limits in $\vec{k}_\parallel$ space. Assuming sampling of a square area of side a with N points per line, the spatial frequency of sampling is a/N, and hence according to the Nyquist criterion, to avoid aliasing effects, only structures of $k_\parallel<\pi N/a$ should be sampled. For acoustic slowness of the order of 0.2 μs/mm, $N=1024$, and propagation distance 10 mm, this limits the frequency to the region $f<N/(2sa)=256$ MHz. Experiments at higher frequencies may be simulated by increasing the value of N, or to some extent by reducing the propagation angle or narrowing the windowing function H.

D. Numerical simulation of forward propagation

By application of the method described above, one is able to perform numerical simulations of wave propagation, having the freedom to choose many parameters: type and size of crystal, wave polarization, type and distribution of the exciting force, etc. We present here the results of calculations for wave fields generated by a point source. The examples have been chosen to show the potential of the forward-propagation technique and to produce results comparable to those available in the literature or analyzed earlier by the authors.

Figure 2 depicts $\tilde{G}_{33}(\vec{x}_\parallel)$ in the plane $x_3=20$ mm for an (001)-oriented silicon crystal, for $f=10$ MHz (a) and (b), 50 MHz (d) and infinite frequency (e). The calculations are for the ST branch and are thus relevant to existing experimental data pertaining to finite wave trains and time gating to separate the faster L wave train from the other two. The FT branch in the vicinity of the $\langle 100\rangle$ axes of crystals such as Si is almost perfectly shear horizontally (SH) polarized and so is not coupled to by the axial excitation discussed here.[11] Extensive studies of internal diffraction patterns by Wolfe and co-worker[2–4] and Wuerz *et al.*[12] have concentrated on the ST internal diffraction pattern, for which the amplitude distribution reveals an abundance of structure absent from the L pattern.

The amplitude images in Figs. 2(a) and 2(d) are essentially identical to the experimental and calculated images of Si reported by Weaver, Hauser, and Wolfe[13] for the same parameters. Their experimental setup is the same as that shown in Fig. 1, and as explained in Sec. II, the insonification by a pressure wave through water delivers a pointlike force normal to the surface. The infinite-frequency intensity plot (e) matches very closely the measured ST component of the phonon focusing pattern of Si.[2]

Comparing Figs. 2(a) and 2(c) we see that as the frequency is raised from 10 to 50 MHz the fringe spacing decreases, and the underlying caustic structure begins to emerge. In the infinite-frequency intensity pattern (e), calculated on the basis of the ray approximation, the caustic structure is fully developed.

Figure 2(g) shows the response to a 15-MHz tone burst of 8 periods. This is intermediate between monochromatic and

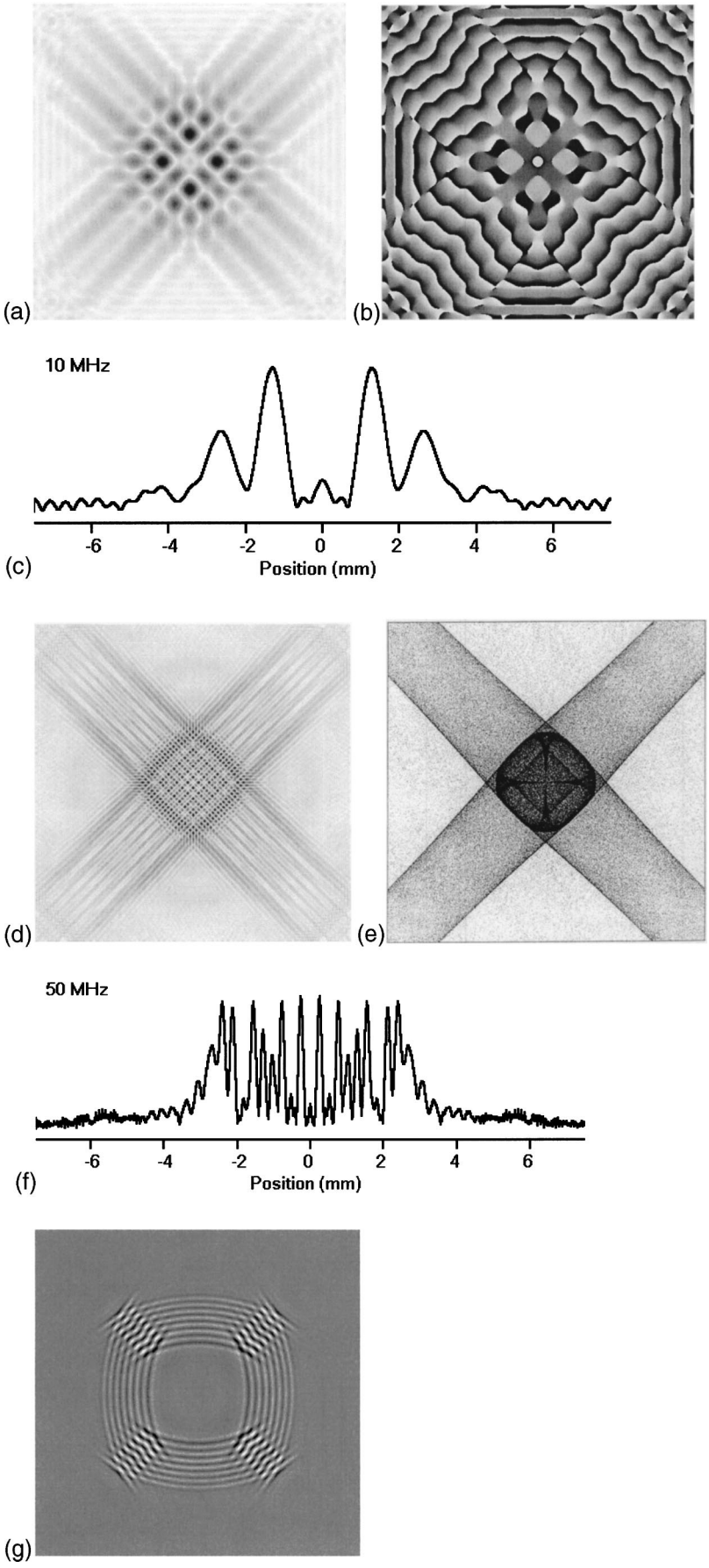

FIG. 2. (a) Amplitude and (b) phase images of silicon, representing the spatial dependence of $\tilde{G}_{33}(\vec{x}_{\parallel})$ in the plane $x_3 = 20$ mm and for frequency $f = 10$ MHz. (d) Depicts the 2D amplitude variation at 50 MHz and (c) and (f) the amplitude variation along the central line in cases (a) and (d), respectively. (e) The infinite-frequency phonon focusing pattern for Si. (g) Response in the plane $x_3 = 10$ mm to a 15-MHz tone burst of 8 periods as observed after a 2.15-μs delay. The reference axes are aligned along the cubic crystallographic axes, and the spatial range of the scan is 15×15 mm^2 in each case. The darkness of the gray scale in (a) and (d) proportional to the amplitude, in (e) to the intensity, and in (g) to the real part of the analytical signal.

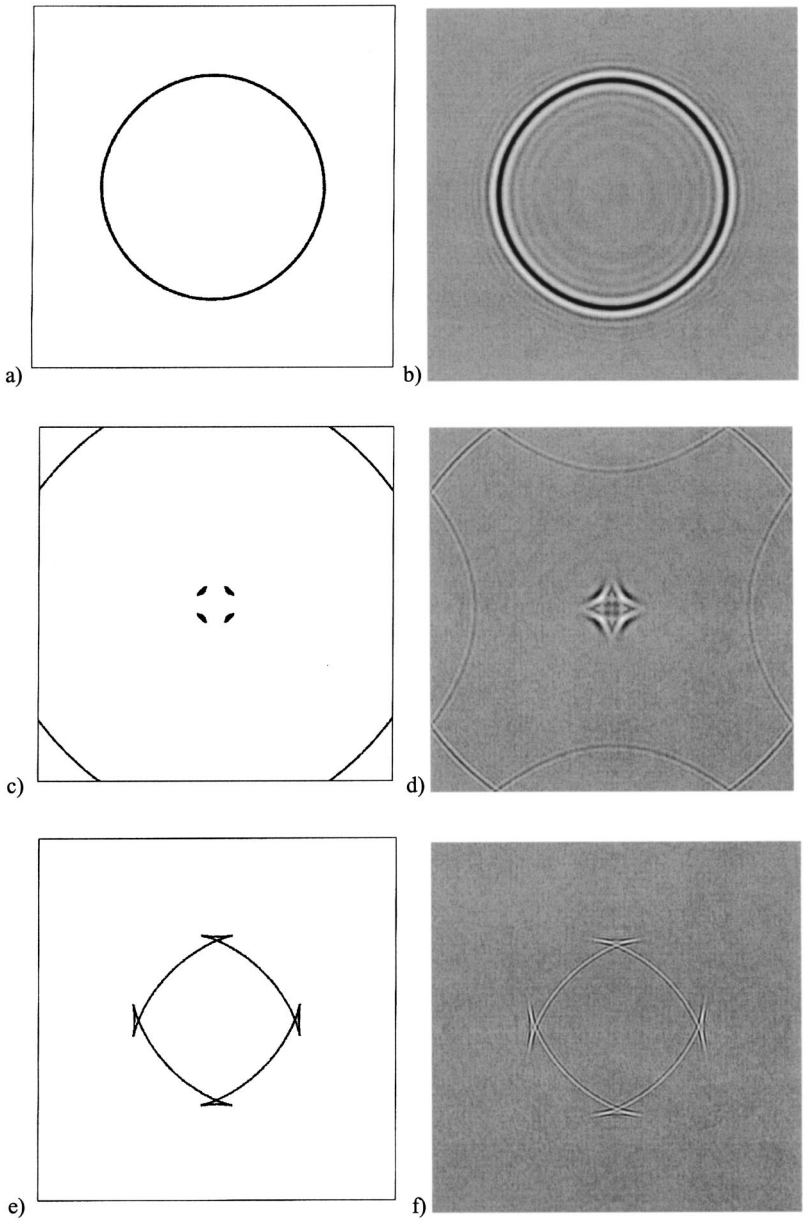

FIG. 3. Numerical simulation of a short-pulse transient signal in a (001)-oriented Si crystal. Scan area $20\times20\ \mathrm{mm}^2$, distance between source and measuring plane $l=10$ mm, delay time $t=1.31\ \mu$s (a) and (b), $t=1.70\ \mu$s (c) and (d), and $t=2.15\ \mu$s (e) and (f). (a), (c), and (e) are for infinite frequency, while the remaining three are for a mean frequency of 30 MHz and bandwidth 12 MHz.

pulse excitation, which we illustrate later. It demonstrates the way interference of the waves creates the internal diffraction pattern. The parameters of the calculation are the same as for those of one of the measurements of Wolfe and Hauser,[4] and the pattern obtained is in good agreement with their measured pattern.

Figure 3 depicts the simulated response of Si in an experiment with short-pulse point excitation for three values of the time delay, 1.31, 1.70, and 2.15 μs. The observation surface area is $20\times20\ \mathrm{mm}^2$, and the observation plane is 10 mm from the excitation point in the [001] direction. These are exactly the parameters of the experimental results on Si reported by Wolfe.[2,3] Figures 3(a), 3(c), and 3(e) are intensity plots for infinite frequency and are calculated in the ray approximation. They essentially represent planar sections at three heights through the L and ST sheets of the group velocity surface. Figures 3(b), 3(d), and 3(f) are the corresponding internal diffraction images representing the real part of the analytical response for the same time intervals and for a pulse of mean frequency 30 MHz and Gaussian envelope of bandwidth 12 MHz. For these latter three images, summation has been performed over all three modes of propagation, but only the L and ST show any visible presence in the images, because the FT mode is so very weakly coupled for axial excitation along the x_3 direction.

It can be seen that the broad-band responses in Figs. 3(b), 3(d), and 3(f) straddle the wave arrivals predicted on the basis of the ray approximation, but as expected they have an oscillatory shape with finite spread because of the limited bandwidth of the excitation. These images compare well with the corresponding experimental images of Wolfe.[2,3] The apparent L wave reflections in Fig. 3(d), i.e., the convex inward circular segments, are an aliasing effect, an artifact of the image sources in neighboring cells, that are inherent to discrete Fourier transforms. They could be eliminated by choosing a larger value of N, but we have left them in be-

cause they resemble the actual L mode side wall reflections present in the measurements of Wolfe.[2,3]

IV. DISTRIBUTED MONOCHROMATIC SOURCE

Hitherto we have been considering a point force. Here we formulate the forward and inverse propagation problems for a planar distributed source and demonstrate the reconstruction of the source structure from complex data collected during PSAM measurements. Generally speaking, in the current experimental approaches one has access only to the x_3 component of the response in the viewing plane, not the full vector response, so rigorous inversion is not possible. Nevertheless, by a procedure akin to synthetic aperture inversion in optics, we are able to achieve a reasonably accurate reconstruction of the source. We discuss the methods of image quality estimation for that technique.

A. Forward propagation

For a force in the x_3 direction with a 2D distribution function in the $x_3=0$ plane $F(\vec{x}_\parallel)\exp(-i\omega t)$, the response in the $x_3=l$ plane is given by the convolution integral

$$u_3(\vec{x}_\parallel,l,\omega)=F(\vec{x}_\parallel)\otimes\tilde{G}_{33}(\vec{x}_\parallel,l,\omega), \tag{7}$$

which may be calculated from the inverse 2D Fourier transform of

$$\overline{u}(\vec{k}_\parallel,l,\omega)=\overline{F}(\vec{k}_\parallel)\cdot\overline{G}_{33}(\vec{k}_\parallel,l,\omega), \tag{8}$$

where $\overline{F}(\vec{k}_\parallel)$ is the 2D Fourier transform of the source structure.

From Eq. (4), it follows for the Fourier domain Green's function that

$$\overline{G}_{33}(\vec{k}_\parallel,l,\omega)\propto\left\{\frac{\Lambda_{33}}{V_3}\exp[i\omega l s_3]\right\}. \tag{9}$$

The angular spectral behavior of relation (9) depends on the propagation mode and type of crystal. For longitudinal waves it is similar to the complex 2D Fresnel function (or Newton's rings) with the shape of the fringes distorted slightly by anisotropy. In the case of the ST mode of a crystal such as Si(001), the amplitude of this function is small in the central area in $\vec{k}_\parallel$ space, approaching zero at $\vec{k}_\parallel=0$, where $U_3=0$, and hence $\Lambda_{33}=0$.

B. Inverse problem

Treating the collected 2D data at the viewing surface as a complex distribution at a synthetic aperture, we invert the propagation process to recover the image of the source by a numerical back propagation technique.[14] To this end, we apply the complex conjugate of relation (9):

$$\overline{G}^{*}_{33}(\vec{k}_\parallel,l,\omega)=\frac{\Lambda_{33}}{V_3}\exp(-ik_3x_3)=\overline{G}_{33}(\vec{k}_\parallel,-l,\omega). \tag{10}$$

The product of Eqs. (8) and (10) yields

$$\overline{u}'(\vec{k}_\parallel,l,\omega)=\overline{u}(\vec{k}_\parallel,l,\omega)\frac{\Lambda_{33}}{V_3}\exp(-ik_3l)=\overline{F}(\vec{k}_\parallel)\left[\frac{\Lambda_{33}}{V_3}\right]^2. \tag{11}$$

Applying the inverse 2D Fourier transform we obtain the image of the source

$$F'(\vec{x}_\parallel)=F(\vec{x}_\parallel)\otimes\mathrm{PSF}(\vec{x}_\parallel), \tag{12}$$

where the point spread function (PSF)

$$\mathrm{PSF}(\vec{x}_\parallel)=\int d\vec{k}^2_\parallel\left[\frac{\Lambda_{33}}{V_3}\right]^2\exp(i\vec{k}_\parallel\cdot\vec{x}_\parallel) \tag{13}$$

is a characteristic of the entire imaging process (including forward wave propagation and calculated inversion) and is to be interpreted as the image of an elementary point source.

C. Imaging quality

The process of measurement through a crystal and numerical reconstruction of a planar source or structure can be treated as a stationary and linear imaging process in two dimensions. A measure of the quality of the imaging is the modulation transfer function[15] (MTF), defined in *k*-vector or spatial frequency space as the modulus of the Fourier transform of the PSF. The MTF is influenced by the apertures of the two transducers, the transmission coefficients at the surfaces, and the $\vec{k}_\parallel$ dependence of $\overline{G}_{33}$. Bearing in mind the fact that the first two factors have a relatively small influence on the results in comparison with the last one, and reiterating our desire to focus on principles rather than detail, we will discuss below only the image quality limitations associated with $\overline{G}_{33}$. Applying the definition of the MTF to Eq. (13) we obtain

$$\mathrm{MTF}(\vec{k}_\parallel)=\left[\frac{\Lambda_{33}(\vec{k}_\parallel/\omega)}{V_3(\vec{k}_\parallel/\omega)}\right]^2. \tag{14}$$

In case of observation by means of the ST mode, low spatial frequencies are represented by *k* vectors close to the $\langle 100\rangle$ direction (small $\vec{k}_\parallel$) and are rarely transferred to the image, and so the MTF has the form of a somewhat distorted annular aperture in $\vec{k}_\parallel$ space.

There are other types of inverting functions besides Eq. (10), which for particular types of crystals and specific propagation modes, could lead to broadening of the transferred spatial frequency range and improvements in the MTF and resolution. Such optimization, similar to the problem of apodization in optics, would entail the definition of goal functions and other issues. We do not, however, wish here to get involved in lengthy discussions of inversion techniques and algorithms. Concentrating rather on principles, we will refer only to the back-propagation technique described above. It has the advantage of ensuring that amplitudes of weak, noise-prone components are not amplified, and in numerical simulation allows us to use the same procedure in inversion as in forward propagation, with only a change in sign of the distance parameter *l*. With this approach then, we present below the results of inversion of simulated results for

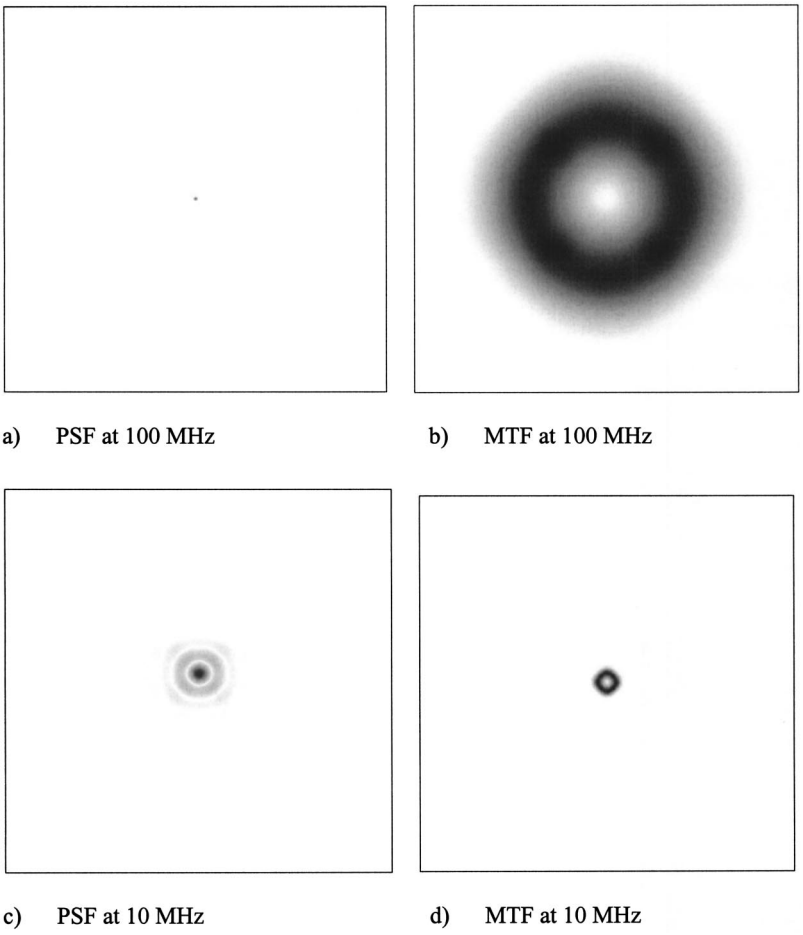

FIG. 4. (a) and (c) PSF and (b) and (d) MTF for the imaging by back propagation of ST waves in silicon at the frequency (a) and (b) 100 MHz and (c) and (d) 10 MHz. The scan range in images (a) and (c) is 15 mm, and in the spatial frequency domain images (b) and (d) is 35 lines/mm. The MTF has a maximum of about 10 lines/mm at 100 MHz and 1 line/mm at 10 MHz.

point and extended sources, and treat an example of inversion of measured data for a pointlike source.

Figure 4 shows the MTF and PSF for 10- and 100-MHz ST waves generated by a point source in a (001)-oriented Si crystal of 15-mm thickness. It depicts the expected dependence of the resolution on the measurement frequency. Extrapolating on this basis, one infers that micrometer resolution could be achieved by going to a frequency of a few gigahertz.

As a demonstration of the potential imaging quality achievable with PSAM in conjunction with a FFT inversion, we present in Fig. 5 simulated image reconstructions, using L and ST waves, of an object in the form of a sinusoidal Siemens star, which is a standard object for the testing of optical systems.

Despite the frequency being the same in both cases, the difference in resolution is quite striking. As expected, because at the same frequency L waves are faster and have longer wavelengths than ST waves, they achieve lower resolution. This is reflected in the blurred central fine-structure region, which covers a larger area for the L waves. On the other hand, since the ST waves in Si(001) tend not to transmit low spatial frequencies, because for these Λ_{33} is small, the outer more broadly structured regions of the test star are obscured in that case.

V. EXAMPLE OF ELASTIC CONSTANT DETERMINATION

The point spread function given by Eq. (13) relates to ideal conditions, in the sense that the same crystal model applies to the forward and inverse transforms. When the forward propagation is experimentally measured or, for whatever reason, does not correspond to the inverse model, then a less-than-ideal PSF is obtained. This fact can be exploited in inverse problem solving. Thus, for inversion of experimental data to obtain elastic constants, we perform the following steps:

(1) Calculate the Fourier transform of the measured complex distribution, which we call $\overline{G}_{33}^{\mathrm{meas}}(\vec{k}_{\parallel},l,\omega)$ and which we interpret as the Fourier domain Green's function of the actual system.

(2) Generate the model inverse distribution $\overline{G}_{33}^{*}(\vec{k}_{\parallel},l,\omega)$, based on assumed crystal characteristics.

(3) Multiply the above two functions.

(4) Perform an inverse Fourier transformation to get the image of the source.

For a pointlike source, the maximum of the PSF thus obtained is a measure of the 2D correlation between the complex measured signal for the sample and $\overline{G}_{33}(\vec{k}_{\parallel},l,\omega)$ obtained from the numerical model. The maximum is sensitive to the elastic constants used in the calculation, and falls off

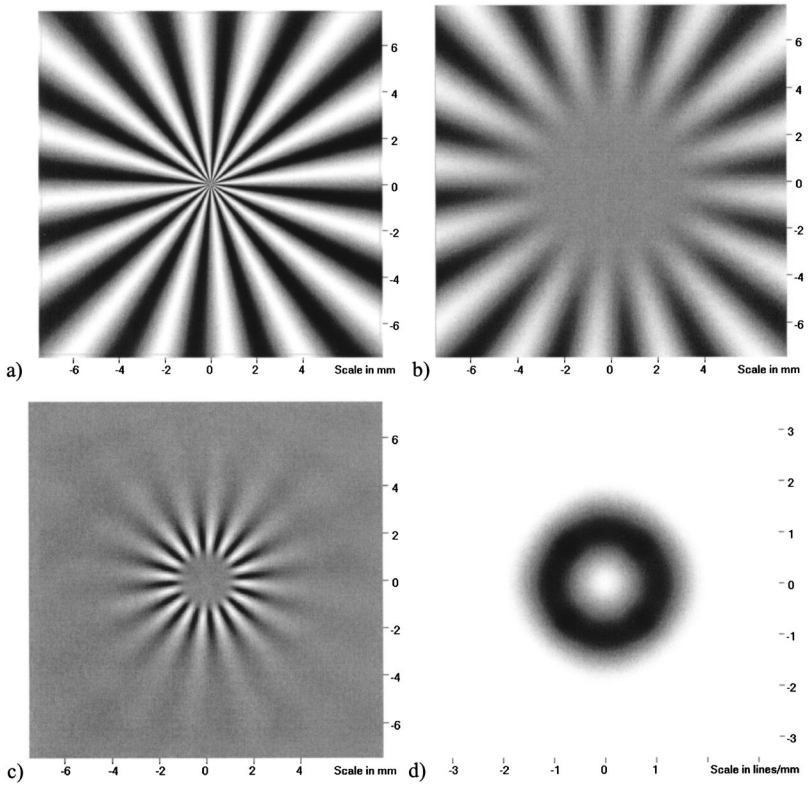

FIG. 5. (a) Numerical image reconstruction of a $1+\sin(16\phi)$ Siemens test star, as measured through a 15-mm-thick silicon crystal at 20 MHz and then reconstructed with back propagation procedures, (b) using L waves and (c) using ST waves. (d) Modulation transfer function shown in spatial frequency space (lines/mm), of the imaging process (propagation and reconstruction) for 20-MHz ST waves. The darkness of the gray scale in (d) is proportional to the amplitude).

rapidly when these deviate from the values pertaining to the specimen.

As an illustration of elastic constant determination using PSAM, we make use of the experimental data shown in Fig. 6(a) for L mode propagation in Si(001), to determine the ''longitudinal'' elastic constant C_{11} of silicon. Figure 6(d) shows the calculated PSF based on known values of the elastic constants C_{12} and C_{44} and three different values of C_{11},

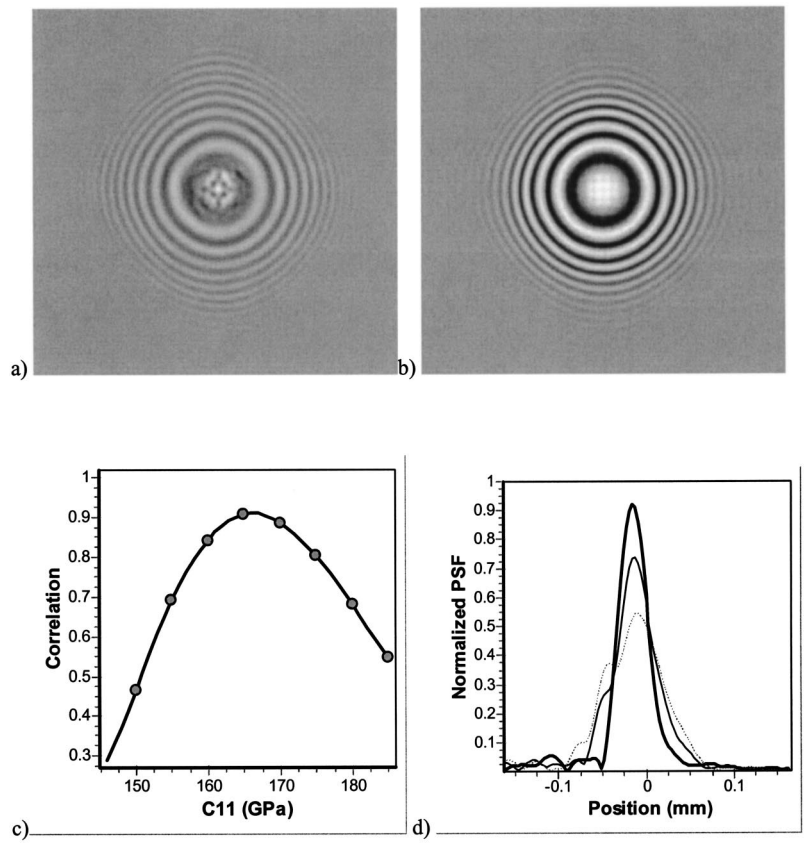

FIG. 6. (a) Real part of the field distribution measured by the PSAM technique at 380 MHz in a (100)-oriented Si crystal of thickness 516 μm, time gated to extract the longitudinal mode and avoid multiple reflections. The horizontal and vertical field size is 1.66 mm. (b) Corresponding simulated pattern using the known elastic constants of Si. (c) Dependence of the correlation between (a) and (b), i.e., peak value of the PSF, on the assumed C_{11} value. (d) PSF cross section for $C_{11}=165$ GPa (thick solid line), 155 GPa (thin solid line), and 150 GPa (dotted line).

to which the data are most sensitive. The PSF for $C_{11} = 165$ GPa, which is close to the known value for Si, is clearly much sharper and has a larger maximum value than the other two. Figure 6(c) shows the variation of the peak height, or correlation value, with assumed value of C_{11}. It shows a clear maximum at the known value of C_{11}. Measurements on both the longitudinal and transverse modes would be required to recover all three elastic constants of silicon.

It is evident from Fig. 6(c), and other estimates of ours concur with this, that PSAM can achieve somewhat better than 1% accuracy in absolute elastic constant determination, which is comparable with that obtained by pulse echo and many other measuring techniques.[16,17] In competition with the well-established standard methods, the niche area we envisage for PSAM is in application to samples that are available in the form of thin plates or even small-angle wedges. The advantages of PSAM in this situation are as follows.

(a) Not much sample preparation is required [in contrast to accurate shaping for resonance experiments, a highly polished surface for surface Brillouin scattering (SBS), accurate parallelism for pulse-echo experiments, etc.].

(b) While our illustrative example above involves only the L mode signal and C_{11}, in general, a single image contains the effects of L, ST, and FT wave propagation in a wide spread of directions and is sensitive to a larger number of elastic constants.

(c) There is no need for attaching transducers to the sample.

(d) Lateral variations of elastic constants in a plate could be easily measured.

(e) Twinning, cracks, and other flaws will show up clearly in PSAM, making it a suitable method for nondestructive testing.

(f) It is a technique that probes bulk elastic constants rather than near-surface elastic constants, as is the case with surface wave techniques, such as laser ultrasound, SBS, and conventional scanning acoustic microscopy.[18]

VI. CONCLUSIONS

We have shown that the angular spectrum method, in conjunction with 2D FFT's, constitutes a computationally very effective means for calculating acoustic wave fields in elastically anisotropic solids. We have treated harmonic as well as more general time-dependent forms of excitation (for which the computational savings are relatively even greater), and have considered both point excitation and distributed sources. We have presented a number of simulated images, which are in good agreement with measurement. Most importantly, we have shown how our FFT approach, when applied to the combined amplitude and phase data obtained with the PSAM technique, provides a very effective means for treating inverse problems such as source reconstruction, image quality assessment, and elastic constant determination.

*On leave from Institute of Physics, Wroclaw University of Technology, Wyb. Wyspianskiego 27, 50-370 Wroclaw, Poland.

[1] W. Grill, K. Hillman, K. U. Wuerz, and J. Wesner, in *Advances in Acoustic Microscopy*, edited by Andrew Briggs and Walter Arnold (Plenum, New York, 1996), Vol. 2.

[2] J. P. Wolfe, Phys. Today **48** (9), 34 (1995).

[3] J. P. Wolfe, *Imaging Phonons* (Cambridge University Press, Cambridge, 1998).

[4] J. P. Wolfe and M. R. Hauser, Ann. Phys. (N.Y.) **4**, 99 (1995).

[5] A. G. Every, K. Y. Kim, and W. Sachse, in *Handbook of Elastic Properties of Solids, Liquids and Gases*, edited by M. Levy, H. E. Bass, and R. Stern (Academic, San Diego, 2001), Vol. I.

[6] Y. Sugawara, O. B. Wright, O. Matsuda, M. Takigahira, Y. Tanaka, S. Tamura, and V. E. Gusev, Phys. Rev. Lett. **88**, 185504 (2002).

[7] A. G. Every and G. M. Amulele, IEEE Trans. Ultrason. Ferroelectr. Freq. Control **49**, 307 (2002).

[8] K. Y. Kim, A. G. Every, and W. Sachse, J. Acoust. Soc. Am. **95**, 1942 (1994).

[9] M. Pluta, M. Shubert, J. Jahny, and W. Grill, Ultrasonics **38**, 232 (2000).

[10] B. A. Auld, *Acoustic Fields and Waves in Solids* (Krieger, Malabar, FL, 1990).

[11] A. G. Every and W. Sachse, Phys. Rev. B **44**, 6689 (1991).

[12] K. U. Wuerz, J. Wesner, K. Hillmann, and W. Grill, Z. Phys. B: Condens. Matter **97**, 487 (1995).

[13] R. L. Weaver, M. R. Hauser, and J. P. Wolfe, Z. Phys. B: Condens. Matter **90**, 27 (1993).

[14] J. Ndop, T. J. Kim, W. Grill, and M. Pluta, Ultrasonics **38**, 166 (2000).

[15] J. W. Goodman, *Introduction to Fourier Optics* (McGraw-Hill, New York, 1996).

[16] *Handbook of Elastic Properties of Solids, Liquids and Gases*, edited by A. G. Every and W. Sachse (Academic, New York, 2001), Vol. I.

[17] A. G. Every and A. K. McCurdy, *Second and Higher Order Elastic Constants, Landolt-Börnstein, New Series, Group III* (Springer, Berlin, 1992), Vol. 29a.

[18] A. G. Every, Meas. Sci. Technol. **13**, R21 (2002).